



# Titanium dioxide/carbon nitride nanosheet nanocomposites for gas phase CO<sub>2</sub> photoreduction under UV-visible irradiation

Angus Crake<sup>a</sup>, Konstantinos C. Christoforidis<sup>a</sup>, Robert Godin<sup>b</sup>, Benjamin Moss<sup>b</sup>, Andreas Kafizas<sup>b</sup>, Spyridon Zafeiratos<sup>c</sup>, James R. Durrant<sup>b</sup>, Camille Petit<sup>a,\*</sup>

<sup>a</sup> Barrer Centre, Department of Chemical Engineering, Imperial College London, South Kensington Campus, London SW7 2AZ, UK

<sup>b</sup> Department of Chemistry, Imperial College London, South Kensington Campus, London SW7 2AZ, UK

<sup>c</sup> Institut de Chimie et Procédés Pour l'Energie, l'Environnement et la Santé, (ICPEES) ECPM, University of Strasbourg, 25 rue Becquerel Cedex 2, Strasbourg, France

## ARTICLE INFO

### Keywords:

Carbon nitride nanosheets

TiO<sub>2</sub>

001 facets

CO<sub>2</sub> reduction

Heterojunction

## ABSTRACT

In the field of photocatalysis and particularly that of CO<sub>2</sub> photoreduction, the formulation of nanocomposites provides avenues to design a material platform with a unique set of structural, optoelectronic and chemical features thereby addressing shortcomings of single-phase materials and allowing synergistic effects. In this work, inorganic/organic composite photocatalysts for CO<sub>2</sub> reduction comprised of titanium dioxide (TiO<sub>2</sub>) and carbon nitride nanosheets (CNNS) were synthesized using a hydrothermal *in-situ* growth method. Specifically, pre-formed CNNS were used to synthesize TiO<sub>2</sub>/CNNS heterostructures with control over the TiO<sub>2</sub> facet formation. This synthesis approach improved the catalytic properties by increasing CO<sub>2</sub> adsorption capacity and facilitating charge transfer. The materials were characterised by various spectroscopic, imaging, and analytical techniques to investigate their structural (from nano- to macroscale), chemical, and optical properties. TiO<sub>2</sub> nanoparticles were efficiently grown on the CNNS. The CO<sub>2</sub> adsorption capacity of the composites was measured, and they were tested for CO<sub>2</sub> photoreduction under UV-Vis illumination with hydrogen as the reducing agent in a heterogeneous gas-solid system to combine CO<sub>2</sub> capture and conversion into a single-step process. Catalytic tests were performed without adding any precious metal co-catalyst. The composites exhibited enhanced CO<sub>2</sub> adsorption capacity and photocatalytic CO<sub>2</sub> conversion compared to their constituent materials (> ten-fold increase) and outperformed the TiO<sub>2</sub> P25 benchmark material. The TiO<sub>2</sub>/CNNS composite with more {001} TiO<sub>2</sub> facets was the most catalytically active. Further investigations using transient absorption spectroscopy (TAS) revealed the control of facet formation improved interfacial transfer at the TiO<sub>2</sub>/CNNS junction. A photocatalytic mechanism was proposed based on the spectroscopic analyses as well as the CO<sub>2</sub> adsorption, and CO<sub>2</sub> conversion results.

## 1. Introduction

With more and more drivers towards increasing the sustainability of our energy resources and production [1], researchers are faced with an unprecedented opportunity to diversify the energy portfolio and increase the share of renewables. Solar fuels – *i.e.* fuels produced using sunlight – represent one of the many routes towards sustainable energy production. One of the key reactions of solar fuels production is the conversion of CO<sub>2</sub> into C<sub>1</sub> and C<sub>1+</sub> energized molecules (*i.e.* CO, CH<sub>4</sub>, CH<sub>3</sub>OH). Overcoming the high thermodynamic and kinetics barriers involved in such reactions can be achieved via a photocatalytic route and improvements towards commercialization rely on the development of efficient and robust photocatalysts. Ideally, these materials should

exhibit: (i) porosity to ensure the concentration of reactants in the vicinity of catalytic sites, (ii) chemical tunability to control the strength of adsorption/desorption of reactants/products, (iii) good light harvesting properties to make use of the solar spectrum, (iv) appropriate catalytic sites and band structure to allow CO<sub>2</sub> reduction reactions to take place and (v) limited charge recombination to promote the formation of reactive charges and enhance efficiency.

Semiconductors are the most extensively investigated photocatalysts for CO<sub>2</sub> reduction. Among them, TiO<sub>2</sub> remains the benchmark owing to its high stability, low cost, and non-toxic nature [2]. Since the seminal demonstration by Fujishima and Honda [3], various strategies have been pursued to improve its photocatalytic activity such as semiconductor coupling, metal ion and nonmetal ion doping, surface

\* Corresponding author.

E-mail address: [camille.petit@imperial.ac.uk](mailto:camille.petit@imperial.ac.uk) (C. Petit).

<https://doi.org/10.1016/j.apcatb.2018.10.023>

Received 6 August 2018; Received in revised form 2 October 2018; Accepted 7 October 2018

Available online 09 October 2018

0926-3373/ © 2018 Elsevier B.V. All rights reserved.

sensitization, and noble metal deposition [4]. The anatase phase is generally the most active, of which, the {001} facet exhibits enhanced activity due to the high density of unsaturated Ti atoms and active surface oxygen atoms [5,6]. Optimisation of {001}/{101} ratio can be achieved by using hydrofluoric acid to control crystal facet formation. This has been shown to greatly improve charge separation via a surface heterojunction where electrons and holes migrate to different facets [6–8]. Despite these advances, the use of  $\text{TiO}_2$  for photocatalytic  $\text{CO}_2$  reduction remains limited due to the large band gap of the material, fast recombination rates of photo-generated charges, and low  $\text{CO}_2$  adsorption capacity [9,10]. Graphitic carbon nitride ( $\text{g-C}_3\text{N}_4$ ) is an alternate metal-free photocatalyst with visible light absorption, chemical and thermal stability and appropriate conduction band level [11–17]. However, it presents high charge carriers recombination rates [18].  $\text{g-C}_3\text{N}_4$  can be exfoliated by various methods to yield carbon nitride nanosheets (CNNS). CNNS are more attractive as photocatalyst compared to bulk  $\text{g-C}_3\text{N}_4$ , owing to longer photogenerated charge lifetimes, and higher surface area [19–22]. The activity of CNNS remains however, considerably low when compared to  $\text{TiO}_2$  [23]. In both  $\text{TiO}_2$  and  $\text{g-C}_3\text{N}_4$  cases, the use of precious metals such as Pt and Pd is usually employed in order to overcome fast recombination processes [18,24].

To take advantage of the complementary features of inorganic and organic photocatalysts, the synthesis of composite hybrid materials has been explored to improve photocatalytic activity with the primary aim of improved charge dynamics and visible-light harvesting [25–34]. Composites of  $\text{g-C}_3\text{N}_4$  and  $\text{TiO}_2$  ( $\text{g-C}_3\text{N}_4/\text{TiO}_2$ ) have shown superior photocatalytic activity by the formation of an artificial photocatalytic Z-scheme. They have been used for various applications including  $\text{CO}_2$  reduction [35–38]. Most prepared  $\text{g-C}_3\text{N}_4/\text{TiO}_2$  heterostructures though used bulk  $\text{g-C}_3\text{N}_4$  and have been synthesised by calcination of  $\text{TiO}_2$  nanoparticles and organic precursor mixtures but are hindered by aggregation and low surface area [9,39]. Instead, using CNNS to form CNNS/ $\text{TiO}_2$  composites should enhance photocatalysis through improved photogenerated charge lifetime owing to the formation of a heterojunction, broader light absorption into visible irradiation from CNNS, and lower  $\text{TiO}_2$  aggregation due to preferential growth onto CNNS resulting in higher surface area and  $\text{CO}_2$  adsorption. The successful synthesis of CNNS/ $\text{TiO}_2$  composites is a challenge, with few reports across various photocatalytic applications [9,39–41] and a single study on  $\text{CO}_2$  reduction (this work involved a Ru(II)–Re(I) binuclear complex). [23] Interestingly, despite the advantages of using CNNS and  $\text{TiO}_2$  crystallites of specific shape (i.e. the exposed facets), such composite materials have never been applied in  $\text{CO}_2$  photocatalytic reduction.

Herein, we report the development of  $\text{TiO}_2$ /CNNS bifunctional nanocomposite materials, with control over the morphology of both  $\text{g-C}_3\text{N}_4$  and  $\text{TiO}_2$ . This photochemical system was selected to demonstrate the  $\text{CO}_2$  capture and conversion as a single process using renewable reductants without the need of expensive co-catalysts.  $\text{TiO}_2$  with preferentially exposed facets were grown on CNNS that provided nucleation sites yielding  $\text{TiO}_2$ /CNNS nanocomposites. This was done to ensure mixing of the two components at the nanoscale, provide strong interfacial interaction and improve charge carrier dynamics. This aspect is particularly important as demonstrated in a previous study [42]. The

prepared nanocomposites presented enhanced surface area (i.e. increased active site exposure),  $\text{CO}_2$  uptake ability and  $\text{CO}_2$  photoreduction. The study demonstrates for the first time photocatalytic  $\text{CO}_2$  reduction for a composite of these materials using  $\text{H}_2$  or  $\text{H}_2\text{O}$  as sacrificial agents in a gas-solid heterogeneous process under UV-visible irradiation. The significant effect of the  $\text{TiO}_2$  crystal shape (i.e. exposed facets) on the photoactivity of the composites is highlighted. The nanocomposites were studied using a variety of analytical, imaging, and spectroscopic techniques. The improved performance was attributed to the complimentary textural, optical, and electronic properties of the materials, and the formation of a heterostructure.

## 2. Experimental section

### 2.1. Material synthesis

All reagents used in this study were of analytical grade and used without further purification. Hydrofluoric acid (48%), melamine (99%) and titanium butoxide (97%) were purchased from Sigma-Aldrich.

#### 2.1.1. Synthesis of carbon nitride nanosheets (CNNS)

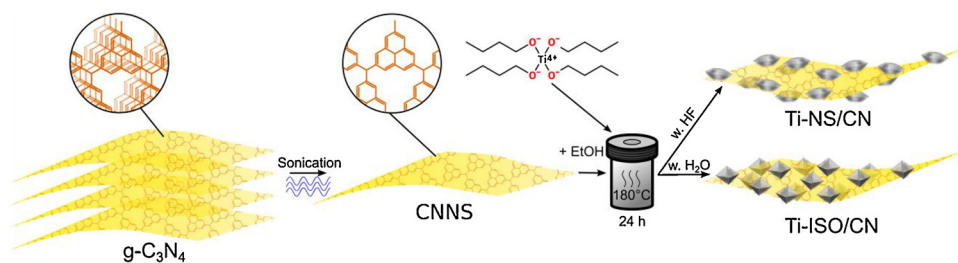
Carbon nitride ( $\text{g-C}_3\text{N}_4$ ) was synthesized from heating melamine in a muffle furnace to  $560^\circ\text{C}$  at a  $5^\circ\text{C}/\text{min}$  ramp under static air for 4 h. Carbon nitride nanosheets (CNNS) were prepared by firstly sonicating the as prepared carbon nitride in water for 4 h. This was centrifuged at 1000 rpm for 10 min, the recovered supernatant was then centrifuged at 12,000 rpm for 30 min to recover CNNS. The CNNS were then dispersed in ethanol by sonication for 4 h and further centrifuged at 2000 rpm for 10 min. The CNNS in the supernatant was then collected. The stock solution of CNNS in ethanol had a CNNS concentration of 2.25 mg/mL, determined by thermogravimetric analysis.

#### 2.1.2. Synthesis of $\text{TiO}_2$

A hydrothermal synthesis was used to produce  $\text{TiO}_2$ . Specifically,  $\text{TiO}_2$  nanosheets ( $\text{TiO}_2\text{-NS}$ , ‘NS’ for nanosheet) were synthesized by adding titanium butoxide (3 mL), hydrofluoric acid (1.2 mL), and ethanol (30 mL) to a PTFE autoclave liner under mixing. The mixture was then heated to  $180^\circ\text{C}$  for 24 h. Following the reaction, the collected material was washed by centrifugation (10,000 rpm for 10 min) with 0.2 M NaOH, then deionized water until a neutral pH was reached, and finally with ethanol prior to drying overnight at  $65^\circ\text{C}$ . For  $\text{TiO}_2$  isometric bipyramidal ( $\text{TiO}_2\text{-ISO}$ , ‘ISO’ for isotropic) synthesis the same procedure was used but 1.2 mL of deionised water was used instead of HF.

#### 2.1.3. Synthesis of $\text{TiO}_2$ /CNNS composites

A hydrothermal *in-situ* synthesis was used to form  $\text{TiO}_2$  in the presence of preformed CNNS to obtain  $\text{TiO}_2$ /CNNS composites as shown in Scheme 1. Titanium butoxide (3 mL), hydrofluoric acid (1.2 mL), and CNNS stock solution (30 mL, i.e. 67.5 mg of CNNS) were added to a PTFE autoclave liner under mixing. The mixture was then heated to  $180^\circ\text{C}$  for 24 h. Hydrofluoric acid was used to control the crystal facet formation and in particular for the development of nanocrystals with exposed {001} facets. Following the reaction, the collected material



**Scheme 1.** Schematic representation of the synthesis process used to produce  $\text{TiO}_2$ /CNNS composites. Following exfoliation of  $\text{g-C}_3\text{N}_4$  to CNNS by sonication,  $\text{TiO}_2$  was synthesised in an autoclave in the presence of CNNS to form  $\text{TiO}_2$ /CN nanocomposites. The  $\text{TiO}_2$  crystal shape was controlled by the addition of either HF or  $\text{H}_2\text{O}$  to the synthesis vessel, leading to the formation of composites with  $\text{TiO}_2$  nanosheets and  $\text{TiO}_2$  isometric structures, respectively.

was washed by centrifugation (10,000 rpm for 10 min) with 0.2 M NaOH, then deionized water until a neutral pH was reached, and finally with ethanol prior to drying overnight at 65 °C. The TiO<sub>2</sub>/CNNS composite synthesised in the presence of HF was named Ti-NS/CN. For synthesis in the absence of HF, named Ti-ISO/CN, 1.2 mL of deionised water used instead of HF. In this study, we assume that the effect of F<sup>−</sup> on the morphology of TiO<sub>2</sub> particles remains the same either for the pure material or the composite material. The expected composition for both composite materials was 95.4 ± 2.0% TiO<sub>2</sub>.

## 2.2. Materials characterization

X-ray diffraction measurements were performed with a PANalytical X'Pert PRO instrument at room temperature (reflection mode at 40 kV and 40 mA using Cu Kα radiation (α<sub>1</sub> = 1.54057 Å, α<sub>2</sub> = 1.54433 Å, weighted average = 1.54178 Å). The interplanar spacing was calculated using Bragg's law:

$$2d \sin \theta = n\lambda$$

Attenuated total reflection Fourier transform-infrared (ATR-FTIR) spectra was collected using a Perkin-Elmer Spectrum 100 Spectrometer equipped with an ATR cell at room temperature. The spectra was generated, collected 8 times, and corrected for the background noise. The experiments were performed using powdered samples, without KBr addition.

Scanning electron microscopy (SEM) images were taken using a high resolution Zeiss Sigma 300 microscope in secondary electron mode (InLens detector). Prior to analysis, the samples were mounted on carbon tape and coated with 20 nm of chromium. Transmission electron microscope (TEM) images were taken by a JEOL 2100Plus instrument at an acceleration voltage of 200 kV, energy dispersive x-ray (EDX) spectroscopy was captured using an Oxford Instruments INCA energy dispersive analytical system. Before analysis, the samples were sonicated in ethanol and then drop casted on a carbon coated copper grid.

Thermogravimetric analysis (TGA) was performed under nitrogen (flowrate 100 mL min<sup>−1</sup>), from 100 to 900 °C at a heating rate of 10 °C min<sup>−1</sup> using a Netzsch TG 209 F1 Libra instrument. Before analysis, the samples were vacuum dried at 120 °C and stored in a desiccator.

Nitrogen adsorption and desorption isotherms were measured using a Micromeritics 3Flex sorption analyser at −196 °C. The surface area was calculated from the Brunauer-Emmett-Teller method [43]. The total volume of pore was calculated from the volume adsorbed at P/P<sub>0</sub> = 0.97. The volume of micropores was determined using the Dubinin-Radushkevich method [44]. The volume of mesopores was calculated as the difference between the total pore volume and the volume of micropores.

Diffuse reflectance ultraviolet-visible (DR-UV/Vis) spectroscopy was measured using a Agilent Cary 500 UV-vis-NIR spectrometer equipped with an integrating sphere. Spectral band width was set to 2 nm, with Spectralon as a standard. Spectra were treated using Kubelka-Munk function [45] in order to eliminate any tailing contribution from the DR-UV-vis spectra. The following equation was applied:  $F(R) = \frac{(1-R)^2}{2R}$  where R is the reflectance. The band-gap (E<sub>g</sub>) values were estimated from the plot of  $F(R)h\nu^{1/n}$  versus energy by extrapolating the linear section.

X-ray photoelectron spectroscopy (XPS) measurements for elemental analysis were performed in an ultrahigh vacuum spectrometer equipped with a VSW Class WA hemispherical electron analyzer. A dual anode Al Kα X-ray source (1486.6 eV) was used as incident radiation and the constant pass energy mode (44 and 22 eV for survey and high resolution spectra respectively) was applied in all XPS measurements. The binding energies (BEs) of all peaks were referenced to the C 1s main peak at 285 eV. The CASA XPS program with a Shirley background subtraction and Gaussian-Lorentzian peak shape was used for the analysis of the peaks. High resolution XPS measurements for band

alignment were performed on a Thermo Scientific K-Alpha spectrometer equipped with an Al Kα X-Ray source (1486.6 eV) and an 180° double focusing hemispherical analyser with a 2D detector at an operating pressure of 1 × 10<sup>−8</sup> mbar as well as a flood gun to minimise charging from photoemission. Powders were mounted onto conductive carbon tape adhered to a sample holder. To further correct for charging, all core lines were corrected a C 1 s (C–C) core line, assumed to be at 284.8 eV. Data was further processed and analysed in the Advantage and CASA XPS software packages.

Transient absorption spectroscopy (TAS) data were acquired on a home-built setup and we used 355 nm excitation pulses of 100 μJ/cm<sup>2</sup> from an Nd:YAG laser (OPOTEK Opolette 355 II, 7 ns pulse width). A broadband probe light was generated from a quartz halogen lamp (Bentham IL1) and long pass filters were placed before the samples to reduce short wavelength irradiation of the sample. To avoid excessive heating, an IR filter consisting of a 5 cm path length cuvette filled with DI water was also placed before the samples. The light was collected in diffuse reflectance mode by a 2" diameter, 2" focal length lens and relayed to a monochromator to select the probe wavelength. A long pass filter was positioned at the entrance of the monochromator to block scattered laser light. The collected light was focused onto a Si photodiode detector (Hamamatsu S3071). Sub-ms data were processed by an electronic amplifier (Costronics) and recorded on an oscilloscope. Data on the ms timescale were simultaneously recorded by a DAQ card (National Instruments). Acquisitions were triggered by scatter from the laser excitation measured by a photodiode (Thorlabs DET10 A). A minimum of 64 laser pulses were averaged together and processed using LabVIEW home-built software. The measurements were performed on the powdered samples in air.

## 2.3. CO<sub>2</sub> adsorption and photocatalytic reduction

CO<sub>2</sub> sorption isotherms at 25 °C were measured up to 1 bara using the same instrument as for the porosity analysis. Prior to the measurements, the samples were degassed at 0.2 mTorr, 120 °C for 24 h. A home-built gas-solid reactor setup was used (Fig. S1) [42]. The photocatalysts (25 mg) were deposited on a stainless steel metal disc with a fixed area of 9.6 cm<sup>2</sup>. Research grade (99.999%) CO<sub>2</sub> and H<sub>2</sub> (99.9995%, Peak Scientific PH200 hydrogen generator) were flowed at controlled rates using mass flow controllers (Omega Engineering, 0–50 mL/min). For experiments requiring water vapor, this was generated from a saturator at room temperature (20 °C) providing a CO<sub>2</sub>/H<sub>2</sub>O of around 40. The photoreactor (35 cm<sup>3</sup>) was vacuumed and replenished with reactant gases five times. Then these gases were passed over the catalyst bed in the photoreactor for 15 residence times before it was sealed at 1.25 bara. A CO<sub>2</sub>/H<sub>2</sub> ratio of 1.5 (vol/vol) was used for experiments using both these gases. A xenon arc lamp (150 W, λ > 325 nm, LOT Quantum Design), equipped with a water filter was used as the irradiation source. Evolved gases were detected by a gas chromatograph mass spectrometer system (GC-MS, Agilent Technologies) with hayesep and molecular sieve packed columns in series, a GS-GASPRO capillary column, thermal conductivity (TCD), flame ionisation (FID) and mass selective (MSD) detectors. The stability of the photocatalysts was tested by repeating the above process after each 6 h illumination without opening the photoreactor. Reference reactions were conducted using N<sub>2</sub> instead of CO<sub>2</sub> in the gas mixture. In addition, isotopic tracing experiments were performed with <sup>13</sup>CO<sub>2</sub> (BOC, > 98% atom <sup>13</sup>CO<sub>2</sub> compared to <sup>12</sup>CO<sub>2</sub>, > 99%). TiO<sub>2</sub> P25 was tested in the same conditions for comparison. The error in CO evolution measurements is ± 10%. The turnover number (TON) was calculated as the ratio of number of reacted photoelectrons to number of catalyst exposed sites:

$$\text{TON} = \frac{\text{number of reacted photoelectrons}}{\text{number of exposed catalytic sites}}$$

The quantity of the exposed catalyst sites was calculated considering



the  $\text{TiO}_2$  component has  $5 \times 10^{18} \text{ m}^{-2}$  [46], and the carbon nitride component which had  $2.2 \times 10^{18} \text{ sites/m}^2$  [47]. The number of catalytic sites used here corresponds to the number of OH sites on the surface of  $\text{TiO}_2$  as determined by Boehm titration<sup>32</sup>. The number of carbon nitride sites correspond to one site per melem unit. These values provide an upper bound to the number of active sites.

### 3. Results and discussion

#### 3.1. Structural and chemical characterisation

The  $\text{TiO}_2$ /CNNS composites were synthesized via an *in-situ* route during which  $\text{TiO}_2$ , with or without the stabilizing agent (*i.e.* HF), was formed in the presence of preformed CNNS (see Scheme 1). This was done to ensure nanoscale mixing of the two components and improve charge carrier dynamics [42]. Owing to the strong links between the materials physical/chemical features and their adsorptive and photocatalytic properties, the composites were characterized by a number of techniques to get a representative picture of the materials from the nano- to the microscale.

The presence of  $\text{TiO}_2$  and CNNS in the composites was first assessed using XRD. The patterns of the composites have been compared to those of the parent materials in Fig. 1a.  $\text{TiO}_2$  in the anatase phase was observed for all samples (single phase and nanocomposite materials) either in the presence ( $\text{TiO}_2$ -NS) or absence ( $\text{TiO}_2$ -ISO) of the stabilizing agent [48]. The  $\text{g-C}_3\text{N}_4$  XRD pattern displayed peaks at  $13.0^\circ$  (100), characteristic of 0.680 nm interplanar spacing of the triazine units, and at  $27.4^\circ$  (002), characteristic of 0.322 nm bulk CN interlayer stacking [22,49]. Successful exfoliation of  $\text{g-C}_3\text{N}_4$  to CNNS was evident from the significant decrease in the interlayer stacking peak ( $27.4^\circ$ ) intensity. The  $\text{TiO}_2$ /CNNS composites showed both  $\text{TiO}_2$  and CNNS diffraction patterns. This confirmed that both components were present and that the  $\text{TiO}_2$  synthesis was not altered significantly by the presence of CNNS. The effect of the stabilizing agent (HF) on  $\text{TiO}_2$  facet growth can be observed by comparing the XRD patterns of  $\text{TiO}_2$ -NS and  $\text{TiO}_2$ -ISO. Indeed, the (004) diffraction peak provides an indirect indicator of the abundance of {001} facet. This peak became significantly broader when using HF, indicating an increase of the {001} facets. This is because the {001} facet formation results in a plate morphology [50]. Additionally, the (101) peaks were more intense relative to (004) due to less (001) planes, which is in line with prior studies [6,51].

Further confirmation of the composite formation came from the ATR-FTIR spectroscopy analyses (Fig. 1b).  $\text{g-C}_3\text{N}_4$  showed the expected band vibrations, *i.e.* C=N ( $1627 \text{ cm}^{-1}$ ) and C-N ( $1312 \text{ cm}^{-1}$ ) stretching, as well as out-of-plane C-N bending ( $803 \text{ cm}^{-1}$ ) [19,52,53]. The spectrum of the CNNS matched that of bulk  $\text{g-C}_3\text{N}_4$  showing

exfoliation did not alter its chemical features.  $\text{TiO}_2$  is relatively inactive in the IR region with mostly a broad Ti-O-Ti stretching bands across  $1000\text{--}400 \text{ cm}^{-1}$ . This was evident for both  $\text{TiO}_2$  samples ( $\text{TiO}_2$ -NS and  $\text{TiO}_2$ -ISO) [40]. The band at around  $1630 \text{ cm}^{-1}$  for these samples is assigned to the bending vibration of the O-H bond [54] from surface hydroxyl groups or water molecules. The scarcity of  $\text{TiO}_2$  features in the  $1800\text{--}1000 \text{ cm}^{-1}$  region allows the presence of CNNS in the  $\text{TiO}_2$ /CNNS nanocomposites spectra to be clearly visible in Fig. 1b. In addition, the Ti-O-Ti stretching band ( $1000\text{--}400 \text{ cm}^{-1}$ ) was observed on the composites spectra confirming the presence of  $\text{TiO}_2$  in these samples. The shifts of the CN peaks at  $1627 \text{ cm}^{-1}$  and  $1312 \text{ cm}^{-1}$  towards higher wavenumbers in the composites compared to  $\text{g-C}_3\text{N}_4$  may indicate a chemical interaction between  $\text{TiO}_2$  and the CNNS facilitated by nanocomposite formation.

Investigation of the composition was carried out using XPS and TGA. Using the former technique, the presence of Ti, O, C, and N in the nanocomposites was confirmed (Fig. S2a). Fluorine was not detected in the  $\text{TiO}_2$ -NS and  $\text{TiO}_2$ -NS/CN composite materials using EDX and XPS. The CNNS and pure  $\text{TiO}_2$ -NS were characterized by two dominant contributions, C and N for the CNNS and Ti and O for the  $\text{TiO}_2$ -NS (we note that no nitrogen was detected on  $\text{TiO}_2$ ). The Ti  $2p_{3/2}$  binding energy (BE) for all  $\text{TiO}_2$  containing materials was found at 458.4 eV corresponding to  $\text{Ti}^{4+}$  surface species in  $\text{TiO}_2$  [42]. CNNS presented the typical chemical states of C and N in  $\text{g-C}_3\text{N}_4$ . The N 1s peak of the CNNS appeared at 398.6 eV (Fig. S2b), characteristic of  $\text{sp}^2$  hybridised nitrogen and the major contribution in the C 1s region centered at 288.4 eV was ascribed to  $\text{sp}^2$  bonded carbon ( $\text{N}=\text{C}-\text{N}$ ) [55]. Both  $\text{TiO}_2$ -NS/CN and  $\text{TiO}_2$ -ISO/CN composites presented an N 1s peak center at the same position as the CNNS sample (Fig. S2b). The unchanged BE of both Ti 2p and N 1s in the composites compared with the bare  $\text{TiO}_2$  and CNNS materials, respectively, verified that the crystal structure of the individual parts in the composites was unaltered. This observation suggested the formation of a composite rather than modification of the crystal lattice structure, *i.e.* N doping of  $\text{TiO}_2$  via decomposition of CNNS. This is in line with the ATR-FTIR data presented above. The amount of  $\text{TiO}_2$  in the composites was also measured by TGA under a nitrogen atmosphere (Fig. S3), considering that the decomposition of CNNS occurred around  $500^\circ\text{C}$ . The  $\text{TiO}_2$  content of  $\text{TiNS/CN}$  and  $\text{TiISO/CN}$  composites were 96.2%wt and 97.1%wt - accurate to  $\pm 1\%$ wt.

In addition to the above techniques, which allowed us to gain insights into the bulk structure and chemistry of the composites, SEM and TEM were employed for an in-depth understanding of the nanocomposite formation and details of the  $\text{TiO}_2$  facet growth. SEM of  $\text{TiO}_2$ -NS (Fig. 2a) revealed agglomerated  $\text{TiO}_2$  NS forming large sheets. The average particle size of the  $\text{TiO}_2$ -NS was approximately 20 nm based on TEM (Fig. S4). Lattice spacings corresponding to the (101) and (001)

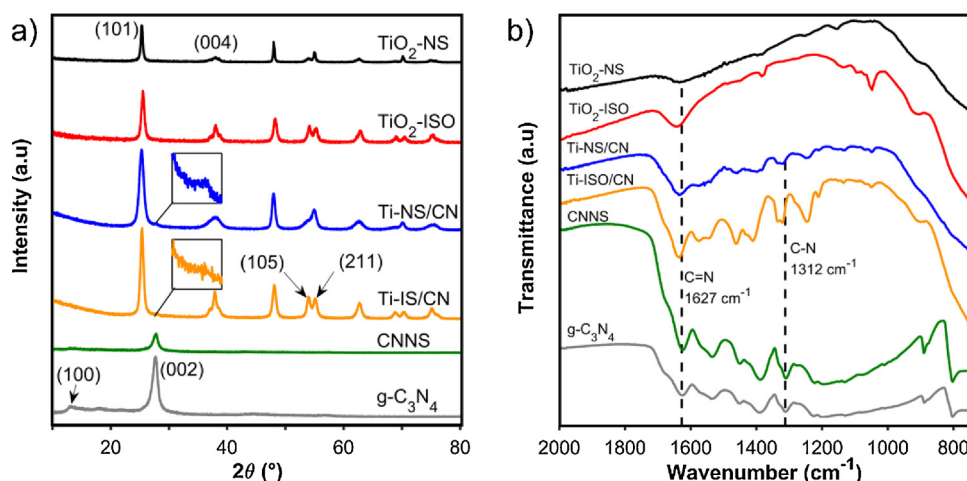
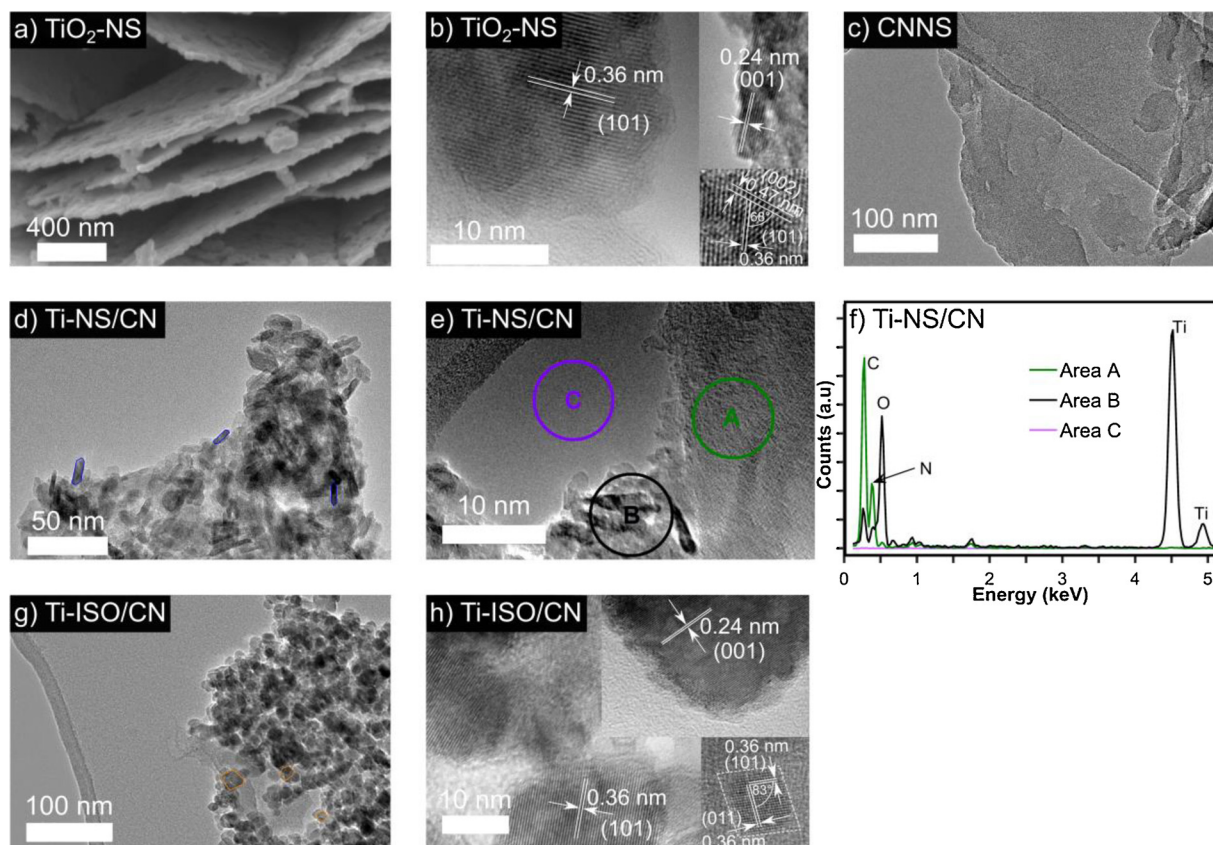


Fig. 1. Material characterization analyses confirming the formation of the  $\text{TiO}_2$ /CNNS composites: a) XRD patterns, b) ATR-FTIR spectra.



**Fig. 2.** EM images of the materials confirming the formation of the composites and highlighting the control over the  $\text{TiO}_2$  morphology: a) SEM image of  $\text{TiO}_2$ -NS; TEM images of b)  $\text{TiO}_2$ -NS, c) CNNS, d) Ti-NS/CN (a couple of  $\text{TiO}_2$  nanoplates are highlighted in blue), e) Ti-NS/CN with uncovered CNNS (Area A),  $\text{TiO}_2$  nanoparticles (Area B), and blank control (Area C – hole of the TEM grid), f) EDX spectra of e), g) Ti-ISO/CN (a couple of  $\text{TiO}_2$  bipyramidal are highlighted in orange), h) Ti-ISO/CN (For interpretation of the references to colour in this figure legend, the reader is referred to the web version of this article).

anatase  $\text{TiO}_2$  planes were measured for the top down and side on views, respectively (Fig. 2b). [51] The interfacial angle between these planes is in agreement with results reported in previous studies on  $\text{TiO}_2$  [56,57]. This confirmed the formation of nanoplatelets with exposed {001} facets [7]. TEM of CNNS also confirmed exfoliation of  $\text{g-C}_3\text{N}_4$  to CNNS; the nanosheets were hundreds of nanometers in length and around 300 nm in width (Fig. 2c). TEM of Ti-NS/CN showed CNNS coated with  $\text{TiO}_2$ -NS particles (Fig. 2d). The  $\text{TiO}_2$  particle size and shape were not affected by the presence of CNNS. Additional evidence of the composite formation was provided by TEM-EDX of Ti-NS/CN (Fig. 2e–f), with images of  $\text{TiO}_2$  particles covering a carbon nitride nanosheet on a nanometer scale. The EDX spectra (Fig. 2f) showed only C and N atoms on the uncovered CNNS region (Area A in Fig. 2e), with predominantly Ti and O atoms on the covered region (Area B in Fig. 2e).

The control of  $\text{TiO}_2$  facet growth, previously suggested by XRD patterns, was further confirmed by TEM of Ti-ISO/CN (Fig. 2g).  $\text{TiO}_2$  nanoparticles deposited onto the carbon nitride nanosheets were observed showing successful nanocomposite synthesis for this composite. Compared to TiNS/CN (Fig. 2d), the morphology of the  $\text{TiO}_2$  crystals was different: an isometric bipyramidal shape was formed, with a smaller average particle size of 15 nm (Fig. S4). HRTEM provided further details of the crystal planes, with a lattice spacing corresponding to the (001) and (101) anatase  $\text{TiO}_2$  planes (Fig. 2h) [51]. The interfacial angle between the (101) and (011) planes aligned with the theoretical value [57]. Overall, TEM provided direct evidence of  $\text{TiO}_2$ /CNNS nanocomposite formation as well as the successful control of  $\text{TiO}_2$  crystal growth. Synthesis in the presence of HF resulted in nanosheet  $\text{TiO}_2$  formation with more {001} facets; while the absence of HF led to the formation of isometric bipyramidal  $\text{TiO}_2$  with more {101} facets.

As mentioned earlier, porosity and surface area are important

aspects of a photocatalyst as it represents a way to enhance interactions between the reactants and the active sites. The textural parameters of the materials are reported in Table S1 (see Fig. S5 for  $\text{N}_2$  isotherms).  $\text{TiO}_2$ -NS exhibited low surface area with some degree of mesoporosity. Considering that no mesopores are expected for single-crystal nanosheets, the observed mesoporosity can be assigned to void space between aggregates of NS.  $\text{TiO}_2$ -ISO exhibited a higher surface area [58] and pore volume comprised of both mesopores and some micropores. We attributed the higher surface area of  $\text{TiO}_2$ -ISO to its smaller particle size and less crystalline nature. Further evidence of exfoliation of  $\text{g-C}_3\text{N}_4$  to CNNS was proven by the threefold increase of surface area of the CNNS [20], and the transition from a Type H4 to H3 hysteresis loop [58]. The surface area and porosity of Ti-NS/CN were enhanced compared to the parent materials. This material exhibited the highest surface area among all. The increased porosity in Ti-NS/CN was assigned to the self-assembly of  $\text{TiO}_2$ -NS in the presence of CNNS forming a porous structure. Such structure is important in photocatalytic reactions providing efficient transport pathways and increasing the concentration of reactants close to active sites. On the other hand, Ti-ISO/CN exhibited an isotherm dominated by the  $\text{TiO}_2$  component with a similar surface area to  $\text{TiO}_2$ . We speculate that the different trends observed for the two types of composites may be due to the distinct morphologies of  $\text{TiO}_2$ -NS and  $\text{TiO}_2$ -ISO:  $\text{TiO}_2$ -NS might allow a particular ‘assembly’ of the  $\text{TiO}_2$  nanosheets and CNNS due to their similar 2D morphology forming meso- and microporous structures with higher surface area.

### 3.2. $\text{CO}_2$ capture

The  $\text{CO}_2$  adsorption capacity of the photocatalysts was measured at 25 °C up to 1 bar (Fig. 3a, Fig. S6). The materials displayed varying  $\text{CO}_2$

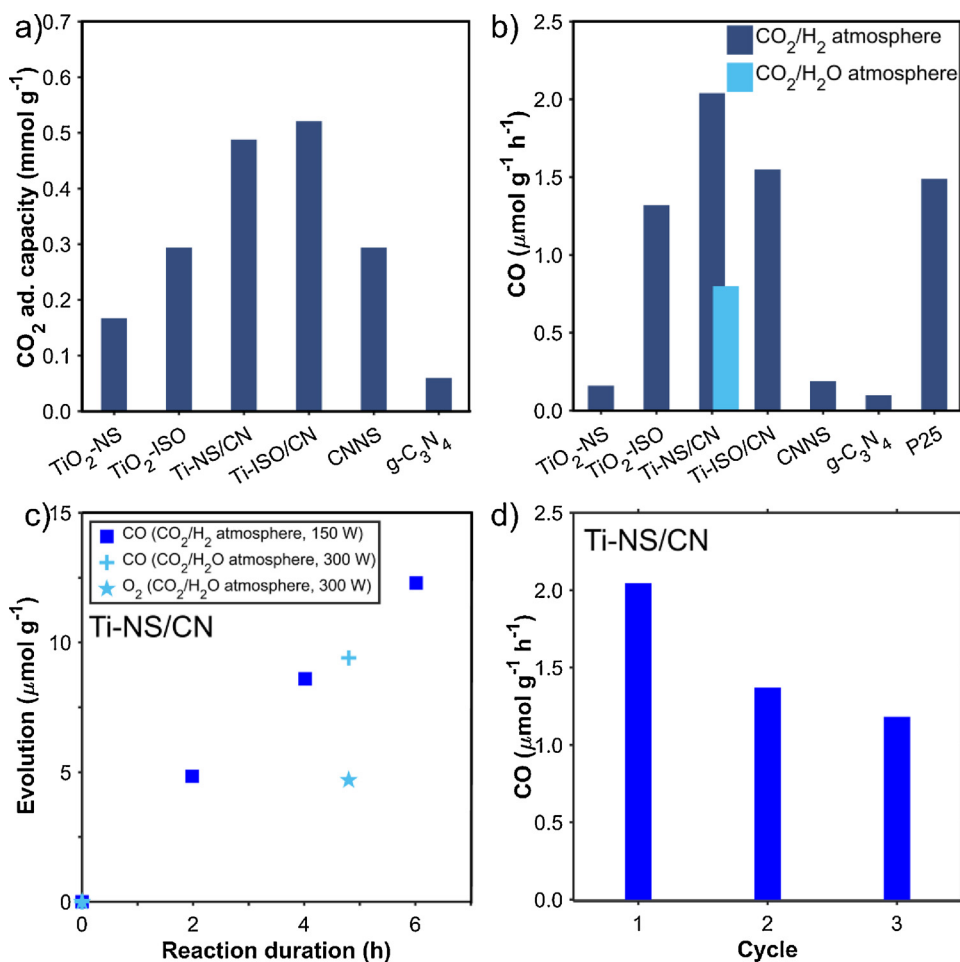


**Fig. 3.** Evaluation of TiO<sub>2</sub>, g-C<sub>3</sub>N<sub>4</sub>, CNNS, and TiO<sub>2</sub>/CNNS composites for: a) CO<sub>2</sub> adsorption at 25 °C, 1 bar, b) CO production. The panel shows CO evolution rates from photocatalytic CO<sub>2</sub> reduction under UV–vis illumination for a duration of 6 h with H<sub>2</sub> or H<sub>2</sub>O as sacrificial agents. The performance of the benchmark TiO<sub>2</sub> P25 material is added for comparison. c) Ti-NS/CN CO evolution over a 6 h photocatalyst test under UV–vis illumination with H<sub>2</sub> and H<sub>2</sub>O as sacrificial agents along with O<sub>2</sub> production after 5 h under UV–vis illumination with H<sub>2</sub>O as sacrificial agent, d) CO evolution for repeated Ti-NS/CN photocatalytic tests under UV–vis illumination with H<sub>2</sub> as the sacrificial agent.

uptakes and the trend followed overall that of surface area. Both TiO<sub>2</sub> materials had a CO<sub>2</sub> adsorption capacity typical for materials of this kind [42]. The slightly higher capacity of TiO<sub>2</sub>-ISO compared to TiO<sub>2</sub>-NS may be related to its higher surface area and more defective nature. The exfoliation of g-C<sub>3</sub>N<sub>4</sub> to CNNS resulted in a five-fold increase in the CO<sub>2</sub> capacity, as reported in other studies [59]. Both nanocomposites exhibited around a twofold increase in CO<sub>2</sub> adsorption compared to their component materials. Ti-ISO/CN exhibited a capacity of 0.521 mmol g<sup>-1</sup> which was similar to that of Ti-NS/CN (0.488 mmol g<sup>-1</sup>), which, given their similar composition, was expected as chemical features take precedence over porosity in controlling CO<sub>2</sub> adsorption at ambient pressure. The small difference observed may be due to a slightly different proportion of reactive sites or access to these sites. The increase in CO<sub>2</sub> uptake for the composite materials is highly desirable, as a higher concentration of CO<sub>2</sub> on the catalyst surface is expected to improve photocatalytic activity [42,60].

### 3.3. Optical and photophysical properties, and photocatalytic CO<sub>2</sub> reduction

Besides CO<sub>2</sub> adsorption, another important property of a photocatalyst is light absorption. This aspect was investigated using UV–vis spectroscopy. The Kubelka-Munk formula was used to convert the data into a Tauc plot (Fig. S7) from which the bandgap energies were measured (Table S2) - the TiO<sub>2</sub> and carbon nitride samples were treated as indirect and direct semiconductors, respectively [20,24,61]. As expected, the TiO<sub>2</sub> samples both exhibited light absorption onsets in the UV region with a bandgap energy around 3.2 eV for anatase TiO<sub>2</sub> [4]. On the other hand, g-C<sub>3</sub>N<sub>4</sub> absorbed in the visible range (bandgap of 2.86 eV). Following exfoliation to CNNS, a blue shift of 0.11 eV was

measured. This shift was expected [62] and was attributed to the quantum size effect in nanostructures, which led to a shift of the valence and conduction bands in opposite directions [22]. The TiO<sub>2</sub>/CNNS composites exhibited light absorption spectra in between those of their TiO<sub>2</sub> and CNNS components.

Considering the light harvesting properties of the materials, they were then tested for CO<sub>2</sub> photocatalytic conversion. Given the nature of the reaction set-up – a heterogeneous gas-solid batch reactor – only gaseous products were analyzed. The tests were carried out under UV–vis illumination, for 6 h, under a CO<sub>2</sub>/H<sub>2</sub> or CO<sub>2</sub>/H<sub>2</sub>O vapor atmosphere. The evolution rates are given in μmol g<sup>-1</sup> h<sup>-1</sup> and μmol m<sup>-2</sup> h<sup>-1</sup> and the TON are calculated (Fig. 3b and Table S3). Under these conditions, all photocatalysts successfully reduced CO<sub>2</sub> into CO. No other CO<sub>2</sub> reduction products were detected in the gas phase. Considering the TiO<sub>2</sub> photocatalysts, TiO<sub>2</sub>-ISO evolved CO at a higher rate than TiO<sub>2</sub>-NS. The trend in performance may seem to contradict our initial claim that {001} facet should lead to an enhanced performance. However, we note that TiO<sub>2</sub>-ISO particles are smaller and adsorb more CO<sub>2</sub> than TiO<sub>2</sub>-NS. For this reason, a direct comparison to highlight the importance of {001} facet is not fair. In addition, an optimisation study of TiO<sub>2</sub> {001}/{101} facet formation has shown high F concentrations to lead to a lower catalytic activity [6,8]. g-C<sub>3</sub>N<sub>4</sub> was the least active material. In comparison, CNNS reduced CO<sub>2</sub> at almost twice the rate, proving that exfoliation leads to a superior photocatalyst. Both TiO<sub>2</sub>/CNNS nanocomposites showed enhanced CO evolution when compared to their components. Ti-NS/CN was observed to be the most active photocatalyst and notably produced CO at a rate over 12 times higher than TiO<sub>2</sub>-NS. A physical mixture of Ti-NS and CNNS with the same composition as Ti-NS/CN evolved CO at the same rate as Ti-NS. This observation showed that the formation of the nanocomposites using an



*in-situ* synthesis had successfully improved the photocatalytic activity. We note that the CO production of Ti-NS/CN was 37% higher than the benchmark material TiO<sub>2</sub> P25 (tested under the same conditions) and higher than rates reported using similar photoreactor systems [63,64]. As the most active photocatalyst, further investigations into the photocatalytic process using Ti-NS/CN were undertaken. Firstly, a control test under a N<sub>2</sub> and H<sub>2</sub> atmosphere for Ti-NS/CN yielded no CO<sub>2</sub> reduction products (Table S3, entry 10). Additionally, isotopic tracing experiments using <sup>13</sup>CO<sub>2</sub> yielded <sup>13</sup>CO (Fig. S8). These analyses prove the photocatalytic origin of CO detected [65]. Kinetic data of the CO evolution from Ti-NS/CN over the 6 h testing period (Fig. 3c) produced a linear progression, indicating a constant catalytic activity. Repeated catalytic tests of Ti-NS/CN (Fig. 3d) showed an initial drop then stabilisation of CO evolution over three cycles, which may due to formation of surface products and the lack of any catalyst regeneration process. Following completion of the above tests, the XRD pattern, the porosity, the UV Vis absorption profile as well the types of chemical bonds were maintained with no significant alteration (Fig. S9), pointing to the robustness of the material.

The influence of the reducing agent was studied by testing Ti-NS/CN with H<sub>2</sub>O vapor (Fig. 3c). Under these conditions, H<sub>2</sub> production from water splitting is a competing side reaction. CO and H<sub>2</sub> were detected at rates of 0.80  $\mu\text{mol g}^{-1} \text{h}^{-1}$  and 2.67  $\mu\text{mol g}^{-1} \text{h}^{-1}$  respectively. This represents a third of the CO production rate obtained when using H<sub>2</sub> as a reducing agent. The generation of photocatalytic oxidation products was also investigated with H<sub>2</sub>O as the reducing agent (Fig. 3c), O<sub>2</sub> was detected (test performed with a 300 W lamp under UV–vis irradiation with water; evolution rates: CO: 1.96  $\mu\text{mol g}^{-1} \text{h}^{-1}$ , O<sub>2</sub>: 0.98  $\mu\text{mol g}^{-1} \text{h}^{-1}$ ).

Considering the above spectroscopic and photocatalytic results, multiple factors could have impacted the photocatalytic activity of the prepared materials. For instance, the surface area played a key role as evidenced by the improvement in CO evolution from exfoliation of g-C<sub>3</sub>N<sub>4</sub> to CNNS, and the high activity of the composite materials. In addition, it is also well known that activity is linked to the ability to photogenerate and separate charges. In the prepared materials, it is likely that a combination of both the enhancement of CO<sub>2</sub> adsorption at the active sites and improved charge separation influenced the photoactivity. Additionally, it was clear the TiO<sub>2</sub> facets in the composites had a large impact on the photocatalytic activity. Whilst the enhanced photocatalytic activity of the TiO<sub>2</sub>/CN composites compared to their parent materials can be explained by complimentary optoelectronic and textural properties (*i.e.* higher surface area, CO<sub>2</sub> adsorption, and higher UV–vis light absorption), the difference in performance between the two composites might be counterintuitive at first since TiO<sub>2</sub>-NS/CN composite performs better than the TiO<sub>2</sub>-ISO/CN composite, yet TiO<sub>2</sub>-ISO proves to be a much better catalyst than TiO<sub>2</sub>-NS. This discrepancy may only be apparent. In fact, we hypothesise that the ‘matching’ morphology of CNNS and TiO<sub>2</sub>-NS is responsible for the higher performance of the related composite. Indeed, TiO<sub>2</sub>-NS presents a two-dimensional (2D) structure, which enables effective contact interface with the 2D morphology of CNNS. This is not the case for TiO<sub>2</sub>-ISO and CNNS. These morphology aspects could have had an impact on the charge dynamics leading to more efficient interfacial charge transfer. As such, a detailed study was undertaken to analyse the photo-excitation and relaxation processes.

Transient absorption spectroscopy (TAS) was used to investigate the photoexcited processes in the TiO<sub>2</sub>/CN composites. TAS can follow the population of excited states over time to give an insight into their nature and timescales of key photophysical processes [66]. Photoexcitation of TiO<sub>2</sub>-NS gave rise to a broad absorption spanning the visible and NIR spectral ranges persisting for hundreds of milliseconds (Fig. 4a). The initial signal, at 1  $\mu\text{s}$ , had a larger amplitude at shorter wavelengths. Over time, the spectra evolved and the dominant signal shifted to longer wavelengths. The spectral signatures of charges in TiO<sub>2</sub> have been well-described and allow us to distinguish between

charge carriers. Holes absorption typically increased toward shorter wavelengths while electron absorption peaked  $\sim 900 \text{ nm}$ . [67] This is consistent with our observations. At early timescales, we observed significant contribution of both hole and electron signals (Fig. 4b). Justified below, the reference electron spectrum was taken as the long-lived signal of TiO<sub>2</sub>, while the reference hole spectra as the long-lived signal of TiISO/CN. Over time, the hole component decreased more quickly compared to the electron signal (Fig. 4a). As balanced electron-hole recombination is expected for TiO<sub>2</sub> [68], we assigned the faster sub-ms decay of holes to scavenging by residual organic surface adsorbates [69]. As a result, only long-lived electrons were observed after hundreds of milliseconds since all holes have been consumed. We note that the influence of these surface organics complicate interpretation of the decay kinetics. We thus limited our analysis to the distinct shape of the TAS spectra for the different samples.

Turning our attention to the Ti-NS/CN composite, we observed much less distinct spectral evolution on the microsecond – millisecond timescales (Fig. S10). While the spectra at longer times were similar to those observed for the TiO<sub>2</sub>-NS sample, in comparison the hole signal at 1  $\mu\text{s}$  was suppressed (Fig. 4c). This suggested a sub- $\mu\text{s}$  hole transfer from the TiO<sub>2</sub> to the CNNS, in line with the favorable energetics from the relative valence band positions of the two materials. The spectra of CNNS alone instead showed a broad absorption peaking between 550–700 nm (Fig. S11) [70]. Here, we considered that the CNNS spectrum was dominated by the electron signal and as such the spectral signature of holes localised on CN was too weak to be observed.

The TiO<sub>2</sub>/CN composite prepared without the stabilizing agent (Ti-ISO/CN) exhibited a spectrum dominated by a signal peaking near 500 nm (Fig. S12). The spectrum did not show temporal evolution, indicating that the same species were dominant throughout the microsecond – millisecond timescales. The shape of the spectra was consistent with a TiO<sub>2</sub> hole signal, and the long-lived signal of Ti-ISO/CN was accordingly taken as the reference hole spectra. As opposed to the TiNS/CN composite, no long-lived electron signal was observed when the stabilizing agent (HF) was omitted, and the initial spectrum was dominated by signal from holes (Fig. 4d). The stabilizing agent thus seems to have played a role in dictating the trapping of charges in the TiO<sub>2</sub>. In the Ti-ISO/CN composite prepared without HF, hole transfer to CN was impeded and holes instead accumulated on TiO<sub>2</sub> leading to low electron concentration in TiO<sub>2</sub>, owing to faster charge recombination, and lower CO<sub>2</sub> reduction yields.

#### 3.4. Proposed reaction pathway

Taking the above results into account, a possible reaction pathway is proposed for photocatalytic CO<sub>2</sub> reduction over Ti-NS/CN (Fig. 5). The band structure was constructed using the bandgap measured in this study (Table S1). The conduction bands were taken from computational studies in literature relative to the SHE of 4.44 eV: -0.96 V for CNNS [71], and 0.28 V for anatase TiO<sub>2</sub> [72]. The band alignment was verified experimentally using high resolution XPS measurements. TiO<sub>2</sub>'s valence band emission produced a shape typical of anatase [73], and presented a Fermi level *c.a.* 3.1 eV above the valence band during the measurement (Fig. S13). The valence band (Fig. S14) of the CNNS is distinct from that of the anatase nanosheets, both in terms of shape and distance from the Fermi level (2.3 eV). The composite Ti-NS/CN displayed identical chemical environments and binding energies to TiO<sub>2</sub> and to the CNNS (Figs. S15–16). This demonstrates that composite formation did not change the chemical nature of the Ti-NS or the CNNS, either by N-doping of the TiO<sub>2</sub> or degradation of the CNNS. The valence band photoemission exhibited a spectrum highly similar to anatase nanosheets both in terms of shape and the relative position of the valence band. This implies that the Fermi level of the anatase nanosheets is largely unaffected upon formation of the Ti-NS/CN composite. This result is broadly consistent with an Ti-NS:CNNS ratio more than 90 % (in favour of Ti-NS) and the strong n-type character of the anatase

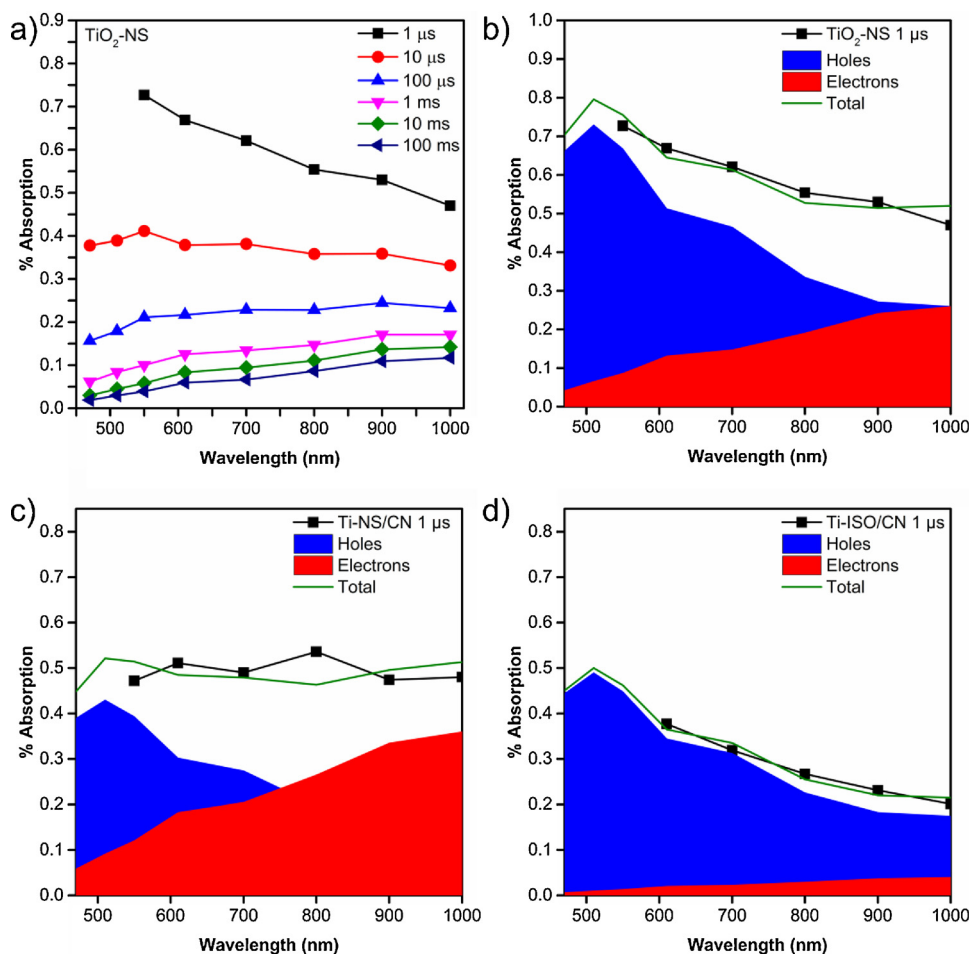


**Fig. 4.** TAS spectra used to study photoexcitation processes in the powdered samples. a) Spectra at different delay times of  $\text{TiO}_2\text{-NS}$  following photoexcitation. b–d) Initial spectra at 1  $\mu\text{s}$  for: b)  $\text{TiO}_2\text{-NS}$ , c)  $\text{Ti-NS/CN}$ , d)  $\text{Ti-ISO/CN}$ . The hole contribution is shaded in blue and the electron contribution is shaded in red. The sum of the two is indicated as the ‘Total’ by a green line, and is compared to the experimental values shown in the black line and squares. All samples were photoexcited by 100  $\mu\text{J}/\text{cm}^2$  pulses of 355 nm laser light (For interpretation of the references to colour in this figure legend, the reader is referred to the web version of this article).

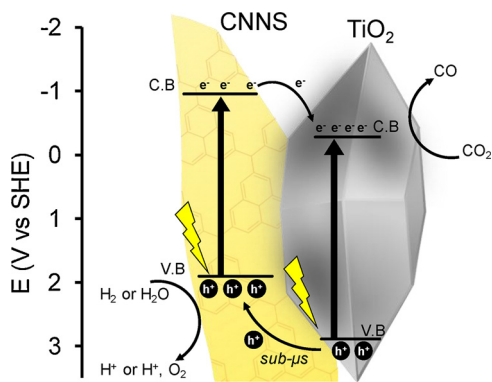


**Fig. 5.** Photocatalytic  $\text{CO}_2$  reduction reaction pathway for the  $\text{TiO}_2/\text{CNNS}$  nanocomposites, improved by hole transfer from  $\text{TiO}_2\text{-NS}$  to CNNS.

nanosheets, as smaller amounts of slightly ‘n-type’ CNNS interfacing with larger quantities of highly n-type  $\text{Ti-NS}$  should be dominated by the chemical potential of the strongly n-doped anatase. The hypothesis that the Fermi level of the  $\text{Ti-NS}$  is largely unaffected upon composite formation can be further interrogated by comparing the oxide O 1s core level spectrum of the anatase nanosheets before and after composite formation. O 1s oxide core levels in metal oxides are broadly insensitive to local changes in bonding (e.g. metal oxidation state). As such, the changes in binding energy – defined as the

difference between the core level energy and the Fermi level energy – of the O 1s oxide core line can be used to measure changes in Fermi level energy that occur upon modifying an oxide [74]. (see supporting information for further details). Within an experimental error of ( $\pm 0.15$  eV), the binding energy of the O 1s oxide peak of the  $\text{Ti-NS}$  is unchanged upon composite formation (Fig. S16), again implying that the Fermi level is not strongly affected by forming a composite with CNNS. Intriguingly, the number of positions of the N 1s environments associated with the CNNS are also unaffected by composite formation. (Fig. S15). This result would suggest that the Fermi level of the CNNS is not strongly affected by composite formation and therefore would imply that the absolute Fermi level energies of the  $\text{Ti-NS}$  and CNNS lie at similar energies.

Using the absolute energy of the anatase conduction band ( $-0.25$  V vs SHE, [75]) to situate the relative energies measured using XPS and optical absorption spectroscopy on an absolute energy scale (SHE scale), a band diagram of the  $\text{Ti-NS/CN}$  system was constructed (Fig. S17). Our estimate of the conduction band energy of CNNS using this method ( $-0.75$   $V_{\text{SHE}} \pm 0.15$   $V_{\text{SHE}}$ ) compares favourably to previously reported values obtained using other techniques [76].

As shown in Fig. 5, the composite heterojunction was Type II. Under UV–vis illumination, both the CNNS and  $\text{TiO}_2$  absorbed photons with sufficient energy to generate electron-hole pairs. Both CNNS and  $\text{TiO}_2$  reduced  $\text{CO}_2$  to CO as both sets of photoexcited electrons possess sufficient electrochemical potential. The enhanced photocatalytic activity of the  $\text{Ti-NS/CN}$  can be explained by two main factors: availability of



CO<sub>2</sub>, and availability of photoexcited electrons. Compared to their constituent materials, CO<sub>2</sub> concentration was increased at the catalytic sites owing to their increased CO<sub>2</sub> adsorption capacity. Recombination of electron-hole pairs was suppressed by interfacial charge transfer via the heterojunction present in this material. This increased the abundance of electrons available for catalysis and resulted in a further increase in CO<sub>2</sub> conversion.

#### 4. Conclusions

The above study presents the design, synthesis, characterisation and testing of inorganic/organic nanocomposites for CO<sub>2</sub> capture and photocatalytic conversion. These composites were formed *via* an *in-situ* synthesis of TiO<sub>2</sub> in the presence of CNNS. Particular attention was paid to controlling the TiO<sub>2</sub> crystal growth and favouring the formation of {001} facets due to their enhanced photocatalytic activity. Electron microscopy imaging and spectroscopic analyses provided direct and indirect indication of the formation of TiO<sub>2</sub> on the CNNS, and demonstrated the control of TiO<sub>2</sub> facet growth. Both nanocomposites showed enhanced CO<sub>2</sub> adsorption capacity and photocatalytic activity (*i.e.* CO photoproduction) compared to their component materials, also exceeding the performance of the TiO<sub>2</sub> P25 benchmark material. CO production using the composites was observed when using either H<sub>2</sub> or water vapour as the sacrificial agent. The TiO<sub>2</sub>/CN with increased number of TiO<sub>2</sub> {001} facets performed better than the composite with isometric TiO<sub>2</sub>. TAS analyses provided insights into the observed catalytic trends. Sub-μs hole transfer from TiO<sub>2</sub> to CN was observed for Ti-NS/CN but not Ti-ISO/CN. This showed the control of TiO<sub>2</sub> crystal growth enabled charge transfer *via* a TiO<sub>2</sub>-CN heterojunction to produce a more active photocatalyst. The study overall demonstrated that the photocatalytic reduction of CO<sub>2</sub> could be improved greatly by forming composite materials with increased CO<sub>2</sub> adsorption capacity and which can suppress electron-hole recombination by facilitation of charge transfer.

#### Acknowledgements

This work was supported by the Engineering and Physical Science Research Council through the First Grant scheme (EP/N024206/1). R.G. thanks the FRQNT for postdoctoral funding. R.G. and J.R.D. acknowledge the support of the ERC AdG Intersolar grant (291482).

#### Appendix A. Supplementary data

Supplementary material related to this article can be found, in the online version, at doi:<https://doi.org/10.1016/j.apcatb.2018.10.023>.

#### References

- [1] M. Mikkelsen, M. Jorgensen, F.C. Krebs, The teraton challenge. A review of fixation and transformation of carbon dioxide, *Energy Environ. Sci.* 3 (2010) 43–81.
- [2] H. Xu, S. Ouyang, L. Liu, P. Reunchan, N. Umezawa, J. Ye, Recent advances in TiO<sub>2</sub>-based photocatalysis, *J. Mater. Chem. A* 2 (2014) 12642–12661.
- [3] A. Fujishima, K. Honda, Electrochemical photolysis of water at a semiconductor electrode, *Nature* 238 (1972) 37–38.
- [4] S.G. Kumar, L.G. Devi, Review on modified TiO<sub>2</sub> photocatalysis under UV/Visible light: selected results and related mechanisms on interfacial charge carrier transfer dynamics, *J. Phys. Chem. A* 115 (2011) 13211–13241.
- [5] X. Han, Q. Kuang, M. Jin, Z. Xie, L. Zheng, Synthesis of titania nanosheets with a high percentage of exposed {001} facets and related photocatalytic properties, *J. Am. Chem. Soc.* 131 (2009) 3152–3153.
- [6] J. Yu, J. Low, W. Xiao, P. Zhou, M. Jaroniec, Enhanced photocatalytic CO<sub>2</sub>-reduction activity of anatase TiO<sub>2</sub> by coexposed {001} and {101} facets, *J. Am. Chem. Soc.* 136 (2014) 8839–8842.
- [7] H.G. Yang, C.H. Sun, S.Z. Qiao, J. Zou, G. Liu, S.C. Smith, H.M. Cheng, G.Q. Lu, Anatase TiO<sub>2</sub> single crystals with a large percentage of reactive facets, *Nature* 453 (2008) 638–641.
- [8] Y. Cao, Q. Li, C. Li, J. Li, J. Yang, Surface heterojunction between {001} and {101} facets of ultrafine anatase TiO<sub>2</sub> nanocrystals for highly efficient photoreduction CO<sub>2</sub> to CH<sub>4</sub>, *Appl. Catal. B: Environ.* 198 (2016) 378–388.
- [9] C. Han, Y. Wang, Y. Lei, B. Wang, N. Wu, Q. Shi, Q. Li, In situ synthesis of graphitic-C3N4 nanosheet hybridized N-doped TiO<sub>2</sub> nanofibers for efficient photocatalytic H<sub>2</sub> production and degradation, *Nano Res.* 8 (2015) 1199–1209.
- [10] K. Li, T. Peng, Z. Ying, S. Song, J. Zhang, Ag-loading on brookite TiO<sub>2</sub> quasi-nanoribbons with exposed {2 1 0} and {0 0 1} facets: activity and selectivity of CO<sub>2</sub> photoreduction to CO/CH<sub>4</sub>, *Appl. Catal. B: Environ.* 180 (2016) 130–138.
- [11] J. Qin, S. Wang, H. Ren, Y. Hou, X. Wang, Photocatalytic reduction of CO<sub>2</sub> by graphitic carbon nitride polymers derived from urea and barbituric acid, *Appl. Catal. B: Environ.* 179 (2015) 1–8.
- [12] J. Sun, J. Zhang, M. Zhang, M. Antonietti, X. Fu, X. Wang, Bioinspired hollow semiconductor nanospheres as photosynthetic nanoparticles, *Nat. Commun.* 3 (2012) 1139.
- [13] Y. Cui, Z. Ding, X. Fu, X. Wang, Construction of conjugated carbon nitride nanoarchitectures in solution at low temperatures for photoredox catalysis, *Angew. Chem. Int. Ed.* 51 (2012) 11814–11818.
- [14] G. Zhang, M. Zhang, X. Ye, X. Qiu, S. Lin, X. Wang, Iodine modified carbon nitride semiconductors as visible light photocatalysts for hydrogen evolution, *Adv. Mater.* 26 (2014) 805–809.
- [15] J. Zhang, G. Zhang, X. Chen, S. Lin, L. Möhlmann, G. Dolega, G. Lipner, M. Antonietti, S. Blechert, X. Wang, Co-monomer control of carbon nitride semiconductors to optimize hydrogen evolution with visible light, *Angew. Chem. Int. Ed.* 51 (2012) 3183–3187.
- [16] Z. Lin, X. Wang, Nanostructure engineering and doping of conjugated carbon nitride semiconductors for hydrogen photosynthesis, *Angew. Chem. Int. Ed.* 52 (2013) 1735–1738.
- [17] J. Zhang, M. Zhang, R.-Q. Sun, X. Wang, A facile band alignment of polymeric carbon nitride semiconductors to construct isotype heterojunctions, *Angew. Chem. Int. Ed.* 51 (2012) 10145–10149.
- [18] Z. Zhao, Y. Sun, F. Dong, Graphitic carbon nitride based nanocomposites: a review, *Nanoscale* 7 (2015) 15–37.
- [19] S. Yang, Y. Gong, J. Zhang, L. Zhan, L. Ma, Z. Fang, R. Vajtai, X. Wang, P.M. Ajayan, Exfoliated graphitic carbon nitride nanosheets as efficient catalysts for hydrogen evolution under visible light, *Adv. Mater.* 25 (2013) 2452–2456.
- [20] P. Niu, L. Zhang, G. Liu, H.-M. Cheng, Graphene-like carbon nitride nanosheets for improved photocatalytic activities, *Adv. Funct. Mater.* 22 (2012) 4763–4770.
- [21] L. Shi, T. Wang, H.B. Zhang, K. Chang, J.H. Ye, Electrostatic self-assembly of nanosized carbon nitride nanosheet onto a zirconium metal-organic framework for enhanced photocatalytic CO<sub>2</sub> reduction, *Adv. Funct. Mater.* 25 (2015) 5360–5367.
- [22] X. Zhang, X. Xie, H. Wang, J. Zhang, B. Pan, Y. Xie, Enhanced photoresponsive ultrathin graphitic-phase C<sub>3</sub>N<sub>4</sub> nanosheets for bioimaging, *J. Am. Chem. Soc.* 135 (2013) 18–21.
- [23] K. Wada, C.S.K. Ranasinghe, R. Kuriki, A. Yamakata, O. Ishitani, K. Maeda, Interfacial manipulation by rutile TiO<sub>2</sub> nanoparticles to boost CO<sub>2</sub> reduction into CO on a metal-complex/semiconductor hybrid photocatalyst, *ACS Appl. Mater. Interfaces* 9 (2017) 23869–23877.
- [24] J. Schneider, M. Matsuoka, M. Takeuchi, J. Zhang, Y. Horiuchi, M. Anpo, D.W. Bahnemann, Understanding TiO<sub>2</sub> photocatalysis: mechanisms and materials, *Chem. Rev.* 114 (2014) 9919–9986.
- [25] X.-H. Li, M. Antonietti, Metal nanoparticles at mesoporous N-doped carbons and carbon nitrides: functional mott-schottky heterojunctions for catalysis, *Chem. Soc. Rev.* 42 (2013) 6593–6604.
- [26] Y.-Y. Cai, X.-H. Li, Y.-N. Zhang, X. Wei, K.-X. Wang, J.-S. Chen, Highly efficient dehydrogenation of formic acid over a palladium-nanoparticle-based Mott-Schottky photocatalyst, *Angew. Chem. Int. Ed.* 52 (2013) 11822–11825.
- [27] J. Fu, J. Yu, C. Jiang, B. Cheng, g-C<sub>3</sub>N<sub>4</sub>-based heterostructured photocatalysts, *Adv. Energy Mater.* (2018) 1701503.
- [28] S. Wang, X. Wang, Photocatalytic CO<sub>2</sub> reduction by CdS promoted with a zeolitic imidazolate framework, *Appl. Catal. B: Environ.* 162 (2015) 494–500.
- [29] X.-J. Sun, D.-D. Yang, H. Dong, X.-B. Meng, J.-L. Sheng, X. Zhang, J.-Z. Wei, F.-M. Zhang, ZIF-derived CoP as a cocatalyst for enhanced photocatalytic H<sub>2</sub> production activity of g-C<sub>3</sub>N<sub>4</sub>, *Sustain. Energy Fuels* 2 (2018) 1356–1361.
- [30] S. Wang, B.Y. Guan, Y. Lu, X.W.D. Lou, Formation of hierarchical In<sub>2</sub>S<sub>3</sub>-CdIn<sub>2</sub>S<sub>4</sub> heterostructured nanotubes for efficient and stable visible light CO<sub>2</sub> reduction, *J. Am. Chem. Soc.* 139 (2017) 17305–17308.
- [31] Y. Chen, G. Jia, Y. Hu, G. Fan, Y.H. Tsang, Z. Li, Z. Zou, Two-dimensional nanomaterials for photocatalytic CO<sub>2</sub> reduction to solar fuels, *Sustain. Energy Fuels* 1 (2017) 1875–1898.
- [32] S. Wang, J. Lin, X. Wang, Semiconductor-redox catalysis promoted by metal-organic frameworks for CO<sub>2</sub> reduction, *Phys. Chem. Chem. Phys.* 16 (2014) 14656–14660.
- [33] S. Wang, W. Yao, J. Lin, Z. Ding, X. Wang, Cobalt imidazolate metal-organic frameworks photolysis CO<sub>2</sub> under mild reaction conditions, *Angew. Chem. Int. Ed.* 53 (2014) 1034–1038.
- [34] S.A. Ansari, M.H. Cho, Growth of three-dimensional flower-like SnS<sub>2</sub> on g-C<sub>3</sub>N<sub>4</sub> sheets as an efficient visible-light photocatalyst, photoelectrode, and electrochemical supercapacitor material, *Sustain. Energy Fuels* 1 (2017) 510–519.
- [35] J. Yu, S. Wang, J. Low, W. Xiao, Enhanced photocatalytic performance of direct Z-scheme g-C<sub>3</sub>N<sub>4</sub>-TiO<sub>2</sub> photocatalysts for the decomposition of formaldehyde in air, *Phys. Chem. Chem. Phys.* 15 (2013) 16883–16890.
- [36] X. Chen, J. Wei, R. Hou, Y. Liang, Z. Xie, Y. Zhu, X. Zhang, H. Wang, Growth of g-C<sub>3</sub>N<sub>4</sub> on mesoporous TiO<sub>2</sub> spheres with high photocatalytic activity under visible light irradiation, *Appl. Catal. B: Environ.* 188 (2016) 342–350.
- [37] M. Reli, P. Huo, M. Šihor, N. Ambrožová, I. Troppová, L. Matějová, J. Lang, L. Svoboda, P. Kuštrowski, M. Ritz, P. Praus, K. Kočí, Novel TiO<sub>2</sub>/C<sub>3</sub>N<sub>4</sub> photocatalysts for photocatalytic reduction of CO<sub>2</sub> and for photocatalytic decomposition of N<sub>2</sub>O, *J. Phys. Chem. A* 120 (2016) 8564–8573.
- [38] J. Yan, P. Li, H. Bian, H. Wu, S. Liu, Synthesis of a nano-sized hybrid C<sub>3</sub>N<sub>4</sub>/TiO<sub>2</sub> sample for enhanced and steady solar energy absorption and utilization, *Sustain.*

- Energy Fuels 1 (2017) 95–102.
- [39] Z. Tong, D. Yang, T. Xiao, Y. Tian, Z. Jiang, Biomimetic fabrication of g-C<sub>3</sub>N<sub>4</sub>/TiO<sub>2</sub> nanosheets with enhanced photocatalytic activity toward organic pollutant degradation, *Chem. Eng. J.* 260 (2015) 117–125.
- [40] Z. Xu, C. Zhuang, Z. Zou, J. Wang, X. Xu, T. Peng, Enhanced photocatalytic activity by the construction of a TiO<sub>2</sub>/Carbon nitride nanosheets heterostructure with High surface Area via direct interfacial assembly, *Nano Res.* 10 (2017) 2193–2209.
- [41] Y. Li, J. Wang, Y. Yang, Y. Zhang, D. He, Q. An, G. Cao, Seed-induced growing various TiO<sub>2</sub> nanostructures on g-C<sub>3</sub>N<sub>4</sub> nanosheets with Much enhanced photocatalytic activity under visible light, *J. Hazard. Mater.* 292 (2015) 79–89.
- [42] A. Crake, K.C. Christoforidis, A. Kafizas, S. Zafeiratos, C. Petit, CO<sub>2</sub> capture and photocatalytic reduction using bifunctional TiO<sub>2</sub>/MOF nanocomposites under UV–vis irradiation, *Appl. Catal. B: Environ.* 210 (2017) 131–140.
- [43] S. Brunauer, P.H. Emmett, E. Teller, Adsorption of gases in multimolecular layers, *J. Am. Chem. Soc.* 60 (1938) 309–319.
- [44] S.G. Chen, R.T. Yang, Theoretical basis for the potential theory adsorption isotherms. The Dubinin-Radushkevich and Dubinin-Astakhov equations, *Langmuir* 10 (1994) 4244–4249.
- [45] P.C. Rao, A.K.S.S. Mandal, Synthesis, structure and band gap energy of a series of thermostable alkaline earth metal based metal-organic frameworks, *CrystEngComm* 16 (2014) 9320–9325.
- [46] H.P. Boehm, Acidic and basic properties of hydroxylated metal oxide surfaces, *Discuss. Faraday Soc.* 52 (1971) 264–275.
- [47] X. Wang, K. Maeda, X. Chen, K. Takanabe, K. Domen, Y. Hou, X. Fu, M. Antonietti, Polymer semiconductors for artificial photosynthesis: hydrogen evolution by mesoporous graphitic carbon nitride with visible light, *J. Am. Chem. Soc.* 131 (2009) 1680–1681.
- [48] K.C. Christoforidis, M. Fernandez-Garcia, Photoactivity and charge trapping sites in copper and vanadium doped anatase TiO<sub>2</sub> nano-materials, *Catal. Sci. Technol.* 6 (2016) 1094–1105.
- [49] X. Wang, K. Maeda, A. Thomas, K. Takanabe, G. Xin, J.M. Carlsson, K. Domen, M. Antonietti, A metal-free polymeric photocatalyst for hydrogen production from Water under visible light, *Nat. Mater.* 8 (2009) 76–80.
- [50] L. Liu, Y. Jiang, H. Zhao, J. Chen, J. Cheng, K. Yang, Y. Li, Engineering coexposed {001} and {101} facets in oxygen-deficient TiO<sub>2</sub> nanocrystals for enhanced CO<sub>2</sub> photoreduction under visible light, *ACS Catal.* 6 (2016) 1097–1108.
- [51] Q. Xiang, K. Lv, J. Yu, Pivotal role of fluorine in enhanced photocatalytic activity of anatase TiO<sub>2</sub> nanosheets with dominant {001} facets for the photocatalytic degradation of acetone in air, *Appl. Catal. B: Environ.* 96 (2010) 557–564.
- [52] J. Xu, L. Zhang, R. Shi, Y. Zhu, Chemical exfoliation of graphitic carbon nitride for efficient heterogeneous photocatalysis, *J. Mater. Chem. A* 1 (2013) 14766–14772.
- [53] S. Zhou, Y. Liu, J. Li, Y. Wang, G. Jiang, Z. Zhao, D. Wang, A. Duan, J. Liu, Y. Wei, Facile in situ synthesis of graphitic carbon nitride (g-C<sub>3</sub>N<sub>4</sub>)-N-TiO<sub>2</sub> heterojunction as an efficient photocatalyst for the selective photoreduction of CO<sub>2</sub> to CO, *Appl. Catal. B: Environ.* 158–159 (2014) 20–29.
- [54] W. Ghann, H. Kang, T. Sheikh, S. Yadav, T. Chavez-Gil, F. Nesbitt, J. Uddin, Fabrication, Optimization and Characterization of Natural Dye Sensitized Solar Cell, 7 (2017) 41470.
- [55] K.C. Christoforidis, M. Melchionna, T. Montini, D. Papoulis, E. Stathatos, S. Zafeiratos, E. Kordouli, P. Fornasiero, Solar and visible light photocatalytic enhancement of halloysite nanotubes/g-C<sub>3</sub>N<sub>4</sub> heteroarchitectures, *RSC Adv.* 6 (2016) 86617–86626.
- [56] D.-N. Pei, L. Gong, A.-Y. Zhang, X. Zhang, J.-J. Chen, Y. Mu, H.-Q. Yu, Defective Titanium Dioxide Single Crystals Exposed by High-energy {001} Facets for Efficient Oxygen Reduction, 6 (2015) 8696.
- [57] L. Gu, J. Wang, H. Cheng, Y. Du, X. Han, Synthesis of nano-sized anatase TiO<sub>2</sub> with reactive {001} facets using lamellar protonated titanate as precursor, *Chem. Commun.* 48 (2012) 6978–6980.
- [58] K.S.W. Sing, F. Rouquerol, J. Rouquerol, P. Llewellyn, 8 - Assessment of Mesoporosity, Adsorption by Powders and Porous Solids, Second edition, Academic Press, Oxford, 2014, pp. 269–302.
- [59] H. Zhang, J. Wei, J. Dong, G. Liu, L. Shi, P. An, G. Zhao, J. Kong, X. Wang, X. Meng, J. Zhang, J. Ye, Efficient visible-light-driven carbon dioxide reduction by a single-atom implanted metal-organic framework, *Angew. Chem. Int. Ed. Engl.* 55 (2016) 14310–14314.
- [60] M. Wang, D. Wang, Z. Li, Self-assembly of CPO-27-Mg/TiO<sub>2</sub> nanocomposite with enhanced performance for photocatalytic CO<sub>2</sub> reduction, *Appl. Catal. B: Environ.* 183 (2016) 47–52.
- [61] J. Zhang, J. Sun, K. Maeda, K. Domen, P. Liu, M. Antonietti, X. Fu, X. Wang, Sulfur-mediated synthesis of carbon nitride: band-gap engineering and improved functions for photocatalysis, *Energy Environ. Sci.* 4 (2011) 675–678.
- [62] J. Ran, T.Y. Ma, G. Gao, X.-W. Du, S.Z. Qiao, Porous P-doped graphitic carbon nitride nanosheets for synergistically enhanced visible-light photocatalytic H<sub>2</sub> production, *Energy Environ. Sci.* 8 (2015) 3708–3717.
- [63] Y. Izumi, Recent advances in the photocatalytic conversion of carbon dioxide to fuels with Water and/or hydrogen using solar energy and beyond, *Coord. Chem. Rev.* 257 (2013) 171–186.
- [64] A.V. Puga, Light-promoted hydrogenation of carbon dioxide—an overview, *Top. Catal.* 59 (2016) 1268–1278.
- [65] I. Grigioni, M.V. Dozzi, M. Bernareggi, G.L. Chiarello, E. Selli, Photocatalytic CO<sub>2</sub> reduction vs. H<sub>2</sub> production: the effects of surface carbon-containing impurities on the performance of TiO<sub>2</sub>-based photocatalysts, *Catal. Today* 281 (2017) 214–220.
- [66] R. Godin, A. Kafizas, J.R. Durrant, Electron transfer dynamics in fuel producing photosystems, *Curr. Opin. Electrochem.* 2 (2017) 136–143.
- [67] X. Wang, A. Kafizas, X. Li, S.J.A. Moniz, P.J.T. Reardon, J. Tang, I.P. Parkin, J.R. Durrant, Transient absorption spectroscopy of anatase and rutile: the impact of morphology and phase on photocatalytic activity, *J. Phys. Chem. C* 119 (2015) 10439–10447.
- [68] A.J. Cowan, J. Tang, W. Leng, J.R. Durrant, D.R. Klug, Water splitting by nanocrystalline TiO<sub>2</sub> in a complete photoelectrochemical cell exhibits efficiencies limited by charge recombination, *J. Phys. Chem. C* 114 (2010) 4208–4214.
- [69] C. Di Valentin, D. Fittipaldi, Hole scavenging by organic adsorbates on the TiO<sub>2</sub> surface: a DFT model study, *J. Phys. Chem. Lett.* 4 (2013) 1901–1906.
- [70] R. Godin, Y. Wang, M.A. Zwijsenburg, J. Tang, J.R. Durrant, Time-resolved spectroscopic investigation of charge trapping in carbon nitrides photocatalysts for hydrogen generation, *J. Am. Chem. Soc.* 139 (2017) 5216–5224.
- [71] H.-Z. Wu, L.-M. Liu, S.-J. Zhao, The effect of Water on the structural, electronic and photocatalytic properties of graphitic carbon nitride, *Phys. Chem. Chem. Phys.* 16 (2014) 3299–3304.
- [72] D.O. Scanlon, C.W. Dunnill, J. Buckeridge, S.A. Shevlin, A.J. Logsdail, S.M. Woodley, C.R.A. Catlow, M.J. Powell, R.G. Palgrave, I.P. Parkin, G.W. Watson, T.W. Keal, P. Sherwood, A. Walsh, A.A. Sokol, Band alignment of rutile and anatase TiO<sub>2</sub>, *Nat. Mater.* 12 (2013) 798–801.
- [73] A.C. Breeson, G. Sankar, G.K.L. Goh, R.G. Palgrave, Phase quantification by X-ray photoemission valence band analysis applied to mixed phase TiO<sub>2</sub> powders, *Appl. Surf. Sci.* 423 (2017) 205–209.
- [74] E.N.K. Glover, S.G. Ellington, G. Sankar, R.G. Palgrave, The nature and effects of rhodium and antimony dopants on the electronic structure of TiO<sub>2</sub>: towards design of Z-scheme photocatalysts, *J. Mater. Chem. A* 4 (2016) 6946–6954.
- [75] S. Burnside, J.-E. Moser, K. Brooks, M. Grätzel, Nanocrystalline mesoporous strontium titanate as photoelectrode material for photosensitized solar devices: increasing photovoltage through flatband potential engineering, *J. Phys. Chem. B* 103 (1999) 9328–9332.
- [76] M.G. Kibria, Z. Mi, Artificial photosynthesis using metal/nonmetal-nitride semiconductors: current status, prospects, and challenges, *J. Mater. Chem. A* 4 (2016) 2801–2820.